nature physics

SUPPLEMENTARY INFORMATION

DOI: 10.1038/NPHYS3559

Coherent cyclotron motion beyond Kohn's theorem

T. Maag[1], A. Bayer[1], S. Baierl[1], M. Hohenleutner[1], T. Korn[1], C. Schüller[1], D. Schuh[1], D. Bougeard[1], C. Lange[1,*], R. Huber[1]

[1]*Department of Physics, University of Regensburg, 93040 Regensburg, Germany*

M. Mootz[2], J. E. Sipe[2,3], S. W. Koch[2], M. Kira[2]

[2]*Department of Physics, Philipps-University Marburg, Renthof 5, 35032 Marburg, Germany*

[3]*Department of Physics and Institute for Optical Sciences, University of Toronto, 60 St. George St., Toronto, Ontario, M5S 1A7, Canada*

*christoph.lange@physik.uni-regensburg.de

Table of Contents

1. Experimental setup 2
2. Sample structure and linear THz response of the magnetically biased 2DEG 2
3. Phase- and amplitude-resolved two-dimensional (2D) terahertz spectroscopy 6
4. Many-body theory of 2DEG 9
5. Kohn's theorem 13
6. Equations of motion 15
7. Description of excitation in a finite excitation spot 16
8. Independence of THz response of spot size 17
9. Coulomb effects on initial state and Kohn's theorem 18
10. Phonon scattering and excitation-induced dephasing 20
11. Classical model 21

DOI: 10.1038/NPHYS3559

1. Experimental setup

We perform phase-locked one- and two-dimensional THz spectroscopy to unravel the coherent nonlinear response of the Landau-quantized electron gas. Our Ti:sapphire laser amplifier provides near-infrared optical pulses centred at a wavelength of 800 nm with a pulse duration of 33 fs and an energy of 5.5 mJ, at a repetition rate of 3 kHz. The pulse train is split into three branches (Fig. S1a) for strong-field THz generation [branch (1)], generation of the THz probe [branch (2)], and electro-optic sampling [branch (3)]. The high-field THz transient labelled A with electric field $\mathcal{E}_{\mathrm{A}}$ (Fig. S1b) is generated by tilted-pulse-front optical rectification in a cryogenically cooled $LiNbO_3$ crystal[S1]. We vary the maximum amplitude $\mathcal{E}_0$ of this waveform in the range of 0.7-8.7 kV/cm using a set of wire-grid polarizers. In branch (2), weak THz transients labelled B whose electric field $\mathcal{E}_{\mathrm{B}}$ has a peak amplitude of 90 V/cm are derived from a 180-μm-thick GaP crystal using optical rectification. These transients are collinearly superimposed with A using a silicon wafer (Si) as a beam combiner. Both THz pulses are focused onto the quantum well sample which is kept at a constant temperature of 4 K in a magnet cryostat. The superconducting magnet provides a homogeneous field which is tunable between 0 and 5 T and is oriented perpendicular to the quantum well plane. Near-infrared pulses in branch (3), finally, serve as an optical gate for electro-optic sampling (EOS) of the transmitted THz waveforms in a 0.5-mm-thick (110)-cut ZnTe crystal[S2,S3]. The x- and y-polarisation components of the THz fields, labelled $\mathcal{E}_x$ and $\mathcal{E}_y$, respectively, are separately analysed using a rotatable wire grid analyser. Two mechanical delay stages (DS) allow us to independently vary the delay time τ between the maxima of the two THz transients A and B, and the electro-optic sampling time t. Two mechanical choppers individually modulate the pulses at sub-harmonics of the laser repetition frequency. This scheme allows us to perform differential detection as described in detail in Supplementary Discussion 3.

2. Sample structure and linear THz response of the magnetically biased 2DEG

Our sample structure (Fig. S2a) was grown by molecular beam epitaxy and hosts two gallium arsenide QWs (blue layers) separated by a 10-nm-thick $Al_{0.24}Ga_{0.76}As$ barrier. The QWs are homogeneously n-doped at a density of $\rho_{\mathrm{e}} = 1.6 \times 10^{11}$ cm^{-2} (electrons visualised as blue spheres) through two remote δ-doping layers which contain the Si donor atoms and are symmetrically located on either side of the QWs, at a distance of 72 nm each (red layers). The resulting two-dimensional electron gases (2DEGs) in the QWs exhibit a high uniformity of ρ_{e}, and an excellent dc mobility

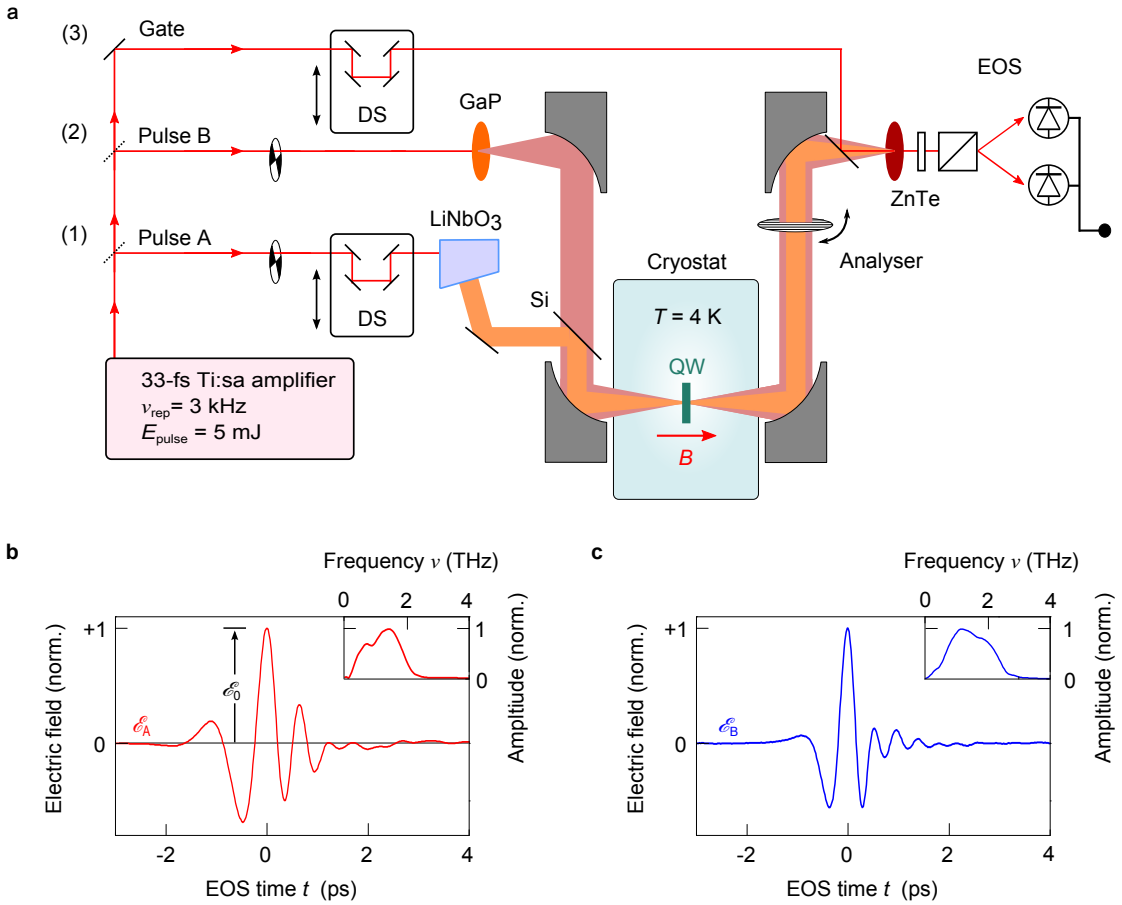

Figure S1 | Experimental scheme and generated few-cycle THz waveforms. a, Setup for two-dimensional THz spectroscopy. DS: variable delay stage, GaP: gallium phosphide crystal, $LiNbO_3$: lithium niobate crystal, Si: silicon wafer, ZnTe: zinc telluride crystal, QW: GaAs quantum well sample, Analyser: THz polarizer, EOS: electro-optic sampling. **b**, THz waveform $\mathcal{E}_A$ of pulse A with variable maximum amplitude $\mathcal{E}_0$. **c**, Waveform $\mathcal{E}_B$ of pulse B with a constant amplitude of 90 V/cm. Insets in **b**, **c**: Corresponding amplitude spectra obtained by Fourier transform of the time-domain signal.

of $\mu = 4.6 \times 10^6$ Vs/cm^2. The band energy offsets are calculated based on literature values for the compounds used in each layer, and plotted in Fig. S2b along the growth direction, with the energy given relative to the Fermi level in the 2DEGs (dashed line). A confinement potential of 220 meV between the QWs and the barriers is achieved. The electron potential in the wells is reduced at the outer interfaces of the QWs, leading to an electron probability distribution $|\Psi(z)|^2$ for the ground-state subband localised accordingly (red curve).

We study the linear optical response of our 2DEGs with the weak THz waveforms $\mathcal{E}_B$ as a function of the magnetic field. A Fourier transform of the electro-optically detected signal yields the transmitted spectral amplitude, which we normalise to the amplitude at zero magnetic bias to obtain the transmission spectrum. A typical transmission spectrum is shown in the inset of Fig. S3

DOI: 10.1038/NPHYS3559

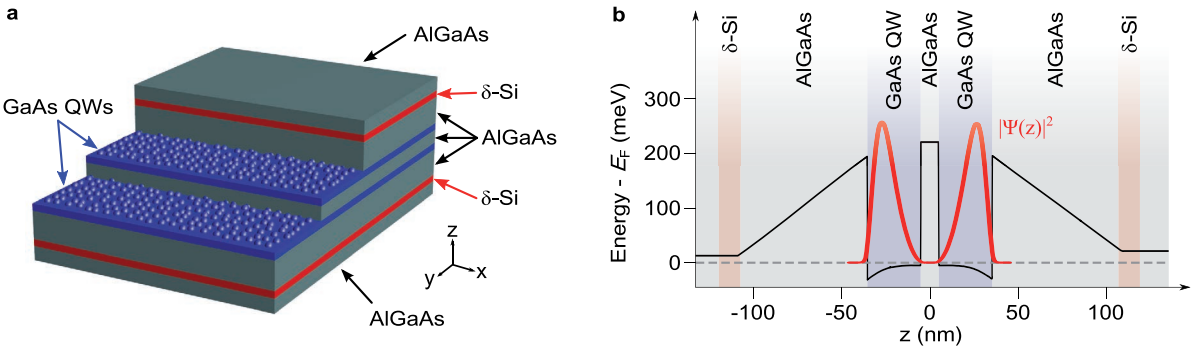

Figure S2 | Sample structure and band offset energy diagram. a, Cut-away view of the sample structure hosting two 2DEGs in GaAs quantum wells (blue layers). The wells, separated by a 10-nm-thick $Al_{0.24}Ga_{0.76}As$ barrier, are homogeneously n-doped at a density of $\rho_e = 1.6 \times 10^{11}$ cm^{-2} per quantum well (blue spheres), and offset from the Si δ-doping layers (red) by 72-nm-thick $Al_{0.24}Ga_{0.76}As$ barriers on either side. **b**, Band offset energies relative to the Fermi level in the 2DEG (dashed line) for the conduction band, in growth direction. Red curve: Probability amplitude of the electron distribution, $|\Psi(z)|^2$.

for a magnetic bias of $B = 3.5$ T. A narrowband, 30 % transmission loss marks the cyclotron resonance frequency $h\nu_c$ (here: $h\nu_c = 1.45$ THz), which scales linearly with the applied magnetic field B (Fig. S3, main panel). From $\nu_c = e\,B/(2\pi m_e)$, we derive an effective mass of $m_e = 0.067 m_0$ consistent with values found in literature[S4], where e is the electric charge and m_0 is the free electron mass.

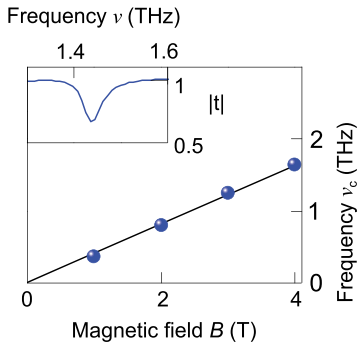

Figure S3 | Scaling of the cyclotron frequency with the magnetic bias field B. Blue dots: measured cyclotron frequency ν_c. Black line: linear fit assuming an effective electron mass of $m_e = 0.067\,m_0$. Inset: transmission spectrum for $B = 3.5$ T.

Effect of tunneling and radiative coupling between two 2DEGs

Increasing the number of 2DEGs improves the signal-to-noise ratio, and consequently the sensitivity in THz spectroscopy. Our sample has two 2DEGs, which is sufficient to clearly detect intriguing many-body nonlinearities beyond Kohn's theorem. Here we show that hypothetical

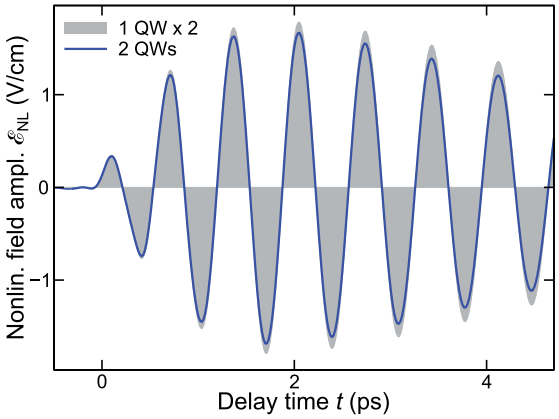

Figure S4 | Nonlinear response of 1 vs. 2 2DEGs. The nonlinear response $\mathcal{E}_{\mathrm{NL}}(t, \tau = 0)$ of a single QW (shaded area, multiplied by 2) is compared with the one of two QWs (solid line); the THz pump field amplitude is $\mathcal{E}_0 = 5.7$ kV/cm.

coupling between the 2DEGs via tunneling, Coulomb interaction, or radiatively is negligible.

To assess tunneling effects between the two 2DEGs, we calculate the tunneling time between them based on the band offset energy diagram and electron distribution shown in Fig. S2b. We find a tunneling time of 1.5 ns which is almost three orders of magnitude larger compared to the typical time scale studied in the experiment. As a result, tunneling between our 2DEGs is negligible. In connection with Supplementary Fig. S7, we also show that the Coulomb coupling between the adjacent 2DEGs can be neglected in our sample. Based on these two results, the total response of our structure should scale roughly linearly with the number of 2DEGs, as long as radiative coupling does not modify the results appreciably.

To study the effect of radiative coupling, we compute the nonlinear response $\mathcal{E}_{\mathrm{NL}}(t, \tau = 0)$ for a single vs. two 2DEGs. Figure S4 compares the nonlinear response of a single 2DEG (shaded area) and two 2DEGs (solid line), both with the same doping density in each quantum well, excited with THz transients with an amplitude of $\mathcal{E}_0 = 5.7$ kV/cm and fully including the self-consistent light–matter coupling in the calculations. To directly compare both cases, we have multiplied the nonlinear signal $\mathcal{E}_{\mathrm{NL}}$ of the single 2DEG by a factor of two. Besides the scaling of the amplitude, $\mathcal{E}_{\mathrm{NL}}$ is only slightly modified by the number of 2DEGs. More precisely, the nonlinear response changes only by a few percent when two 2DEGs are used in the calculations instead of one. Therefore, our experiment essentially accesses physics of a single 2DEG, as we improve the signal-to-noise by using two 2DEGs.

To experimentally confirm that a single 2DEG indeed reproduces the theory prediction, we present an independent set of experiments with a single 2DEG. Using molecular beam epitaxy, we have grown an additional QW sample which hosts a single 2DEG doped at $\rho_{\mathrm{e}} = 6 \times 10^{11}\,\mathrm{cm}^{-2}$ in

DOI: 10.1038/NPHYS3559

a 25-nm wide well, resulting in a filling factor of 4 at a magnetic bias of 3.5 T. The dc mobility of $\mu_{DC} = 1 \times 10^6$ cm^2/Vs is only slightly lower than that of the original sample. This sample allows us to verify that our results depend neither on the number of 2DEGs and possible inter-well coupling, nor on the carrier density, demonstrating the universality of the Coulomb-mediated nonlinearities.

We have performed two-dimensional spectroscopy at two characteristic THz field amplitudes of $\mathcal{E}_A = 0.7$ and 1.4 kV/cm, while the probe field amplitude was again $\mathcal{E}_B = 90$ V/cm. In Fig. S5a,b, the nonlinear signal $\mathcal{E}_{NL}$ is plotted analogously to Figs. 3b-e of the manuscript, i. e., as a function of electro-optic delay time t and delay time τ between pulses A and B, as a colour plot. All fundamental aspects reported in the manuscript are reproduced: Vertical and diagonal phase fronts mark pump–probe signals which appear as distinct features in the corresponding two-dimensional spectral maps (Figs. S5c,d) at frequency tuples $(\nu_t, \nu_\tau) = (\nu_c, 0)$ and $(\nu_t, \nu_\tau) = (\nu_c, -\nu_c)$. Here, ν_t and ν_τ are the frequencies associated with t and τ, and ν_c is the cyclotron frequency. Four-wave mixing causes phase fronts slanted at an angle of 22.5° and is observed in the frequency maps at $(\nu_c, -2\nu_c)$ (Figs. S5c,d). At $\mathcal{E}_A = 0.7$ kV/cm, the coherence of the inter-Landau-level polarization is maintained along τ over the entire window of observation up to $\tau = 4$ ps. For $\mathcal{E}_A = 1.4$ kV/cm, the polarization dephases more rapidly such that the oscillations along τ disappear for $\tau > 2$ ps. Note that the onset of dephasing and nonlinear effects is observed at lower peak amplitudes of the driving field as compared to the double-well sample. This is consistent with the larger doping level and hence filling factor: In order to activate phonon interaction in the highly doped single-well sample, only two LLs need to be traversed. Furthermore, the larger dipole moment associated with the transition from Landau level $n = 4$ to $n = 5$ and the higher carrier density promote stronger light–matter interaction. In conclusion, our two-2DEG system indeed produces qualitatively the same result as a single 2DEG.

3. Phase- and amplitude-resolved two-dimensional (2D) terahertz spectroscopy

Field-sensitive two-dimensional THz spectroscopy allows us to monitor the coherent and incoherent dynamics of the inter-Landau level polarisation at high THz field amplitudes. To this end, the two THz transients A and B are collinearly superimposed, by a Si wafer, and focussed onto the sample. Pulse B is kept fixed in time, whereas pulse A is delayed with respect to pulse B by a variable time τ. The transients are linearly polarised in x- and y-direction, respectively. We measure the y-component of the transmitted electric field $\mathcal{E}^t_{AB}$ using electro-optic detection (see Supplementary Discussion 1). $\mathcal{E}^t_{AB}$ consists of linear and nonlinear contributions of A and B

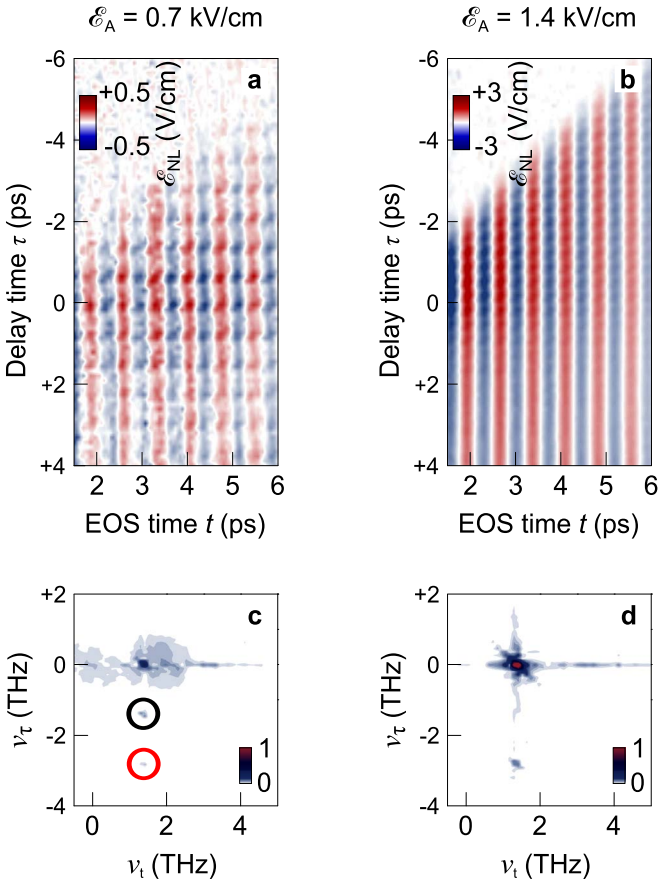

Figure S5 | Two-dimensional nonlinear THz spectroscopy of a highly doped, single quantum well. a,**b** Color plot of the nonlinear field amplitude $\mathcal{E}_{\mathrm{NL}}$ as a function of electro-optic sampling time t, and delay time τ between pulses A and B, for excitation with amplitudes of 0.7 and 1.4 kV/cm. **c**,**d** Fourier transform of data in **a**,**b**, revealing pump–probe (black circles) and four-wave-mixing signals (red circles).

individually, subsumed into $\mathcal{E}^t_{\mathrm{A}}$ and $\mathcal{E}^t_{\mathrm{B}}$, and of nonlinear correlations $\mathcal{E}_{\mathrm{NL}}$ involving at least one photon from each of the two pulses[S5]. The total signal may be written as

$$\mathcal{E}^t_{\mathrm{AB}} = \mathcal{E}^t_{\mathrm{A}} + \mathcal{E}^t_{\mathrm{B}} + \mathcal{E}_{\mathrm{NL}}\,. \tag{1}$$

Using lock-in amplification and differential detection, we first determine $\mathcal{E}^t_{\mathrm{AB}}\,(t,\tau)$, corresponding to the situation where both beams are incident on the sample (Fig. S6**a**). In this two-dimensional data set, $\mathcal{E}^t_{\mathrm{B}}$ is seen as a set of faint vertical lines around an electro-optic sampling time $t = 0$ ps. The waveforms $\mathcal{E}^t_{\mathrm{A}}$, which are delayed by τ, appear as diagonal lines, strongly exceeding $\mathcal{E}^t_{\mathrm{B}}$ in amplitude. In a subsequent step, all contributions originating from pulse A alone are removed by referencing to the signal which is obtained when the chopper in branch (1) blocks the beam, yielding $\mathcal{E}^t_{\mathrm{AB-A}} = \mathcal{E}^t_{\mathrm{AB}} - \mathcal{E}^t_{\mathrm{A}}$ (Fig. S6b). In this setting, $\mathcal{E}^t_{\mathrm{B}}$ represents the contribution strongest

DOI: 10.1038/NPHYS3559

in amplitude. Finally, we isolate the correlated response by further subtracting the remaining single-pulse contribution $\mathcal{E}^t_{\rm B}$ (chopper in branch (2) set to block), and obtain $\mathcal{E}_{\rm NL} = \mathcal{E}^t_{\rm AB} - \mathcal{E}^t_{\rm A} - \mathcal{E}^t_{\rm B}$ (Fig. S6c and manuscript Figs. 3b-e).

The time-domain data in Figs. S6a,b indicate the dominant phase fronts of beams A (diagonal) and B (vertical) in the $t-\tau$-plane, and the corresponding perpendicularly oriented wave vectors. In addition to these lines, the correlated field $\mathcal{E}_{\rm NL}$ reveals pronounced phase fronts under an angle of 22.5° (white line in Fig. S6c), caused by a four-wave mixing process involving two photons from pulse A and one from pulse B. In general, the emanating multi-photon processes can be disentangled by a 2D-Fourier transformation of $\mathcal{E}_{\rm NL}$ which yields the corresponding spectral amplitude as a function of the frequencies ν_t and ν_τ associated with t and τ, respectively. The spectra, plotted for a series of amplitudes of beam A in the manuscript in Figs. 3h-k, exhibit strong signatures at spectral locations where ν_t and ν_τ are integer multiples of the cyclotron frequency. The signatures directly represent the wavevector sum of the contributing fields for the respective nonlinear process[S5]. The constituent wavevectors for the most prominent nonlinear contributions are listed in Table S1. We note that in the nonperturbative regime, each process may contain higher-order contributions arising from more complex paths through the Liouville space than the direct sums listed in the table.

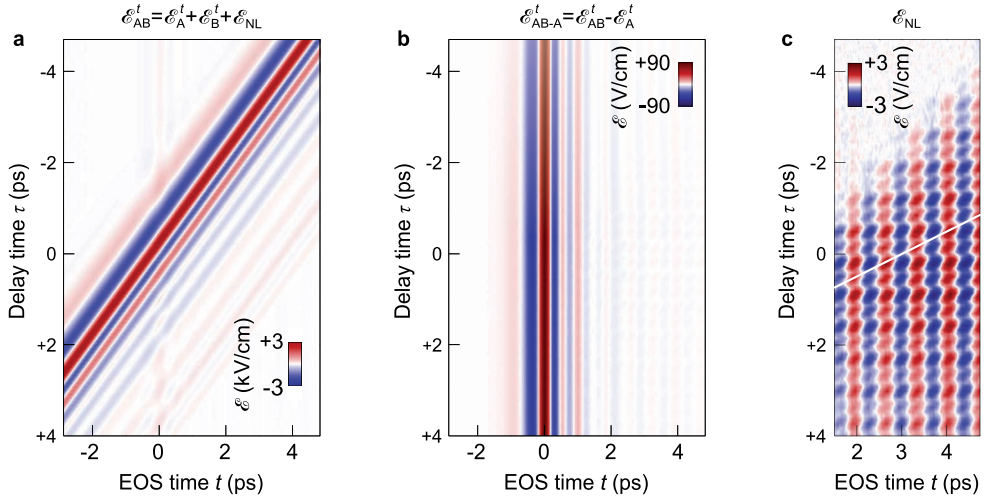

Figure S6 | 2D-THz transmission as a function of EOS time t and relative delay τ. **a**, Transmitted electric field $\mathcal{E}^t_{\rm AB}(t,\tau)$ when both beams A and B are switched on. **b**, THz field $\mathcal{E}^t_{\rm AB-A}(t,\tau)$ after subtraction of the contribution of beam A. **c**, $\mathcal{E}_{\rm NL}(t,\tau)$ arising from nonlinear interactions between A and B alone. White slanted line: guide to the eye for the phase fronts corresponding to one of the four-wave mixing processes.

Nonlinear process	Wave vector	Frequencies ν_t	ν_τ
Pump–probe	$k_{\mathrm{p1}} = k_{\mathrm{A}} - k_{\mathrm{A}} + k_{\mathrm{B}}$	ν_{c}	0
	$k_{\mathrm{p2}} = k_{\mathrm{B}} - k_{\mathrm{B}} + k_{\mathrm{A}}$	ν_{c}	-ν_{c}
Four-wave mixing	$k_{41} = 2k_{\mathrm{B}} - k_{\mathrm{A}}$	ν_{c}	ν_{c}
	$k_{42} = 2k_{\mathrm{A}} - k_{\mathrm{B}}$	ν_{c}	$-2\nu_{\mathrm{c}}$
Six-wave mixing	$k_{61} = 3k_{\mathrm{A}} - 2k_{\mathrm{B}}$	ν_{c}	$-3\nu_{\mathrm{c}}$

Table I | Wavevectors and frequencies of the main nonlinear processes contributing to $\mathcal{E}_{\mathrm{NL}}$.

4. Many-body theory of 2DEG

To explain the experimental observations, we present a brief overview of our full many-body theory[S6,S7] including all relevant interactions among the charge carriers. We follow the standard description of Landau electrons[S8] in a static magnetic field, by using the minimal substitution[S8]

$$\hat{H} = \frac{1}{2m_e}\left(\hat{\mathbf{p}} + |e|\mathbf{A}_{\mathrm{stat}}(\mathbf{r})\right)^2 , \tag{2}$$

where m_{e} is the effective electron mass and e denotes the elementary charge. The vector potential $\mathbf{A}_{\mathrm{stat}}(\mathbf{r}) = \frac{1}{2}\mathbf{B}\times\mathbf{r}$ is described in the symmetric gauge with a static magnetic field $\mathbf{B}$ pointing perpendicular to the 2DEG direction, i. e., the z-direction, $\mathbf{B} = B\,\mathbf{e}_z$. By separating $\mathbf{r} = (\mathbf{r}_\parallel, z)$, the eigenfunctions of $\hat{H}$ yield the standard Landau electron solutions in polar coordinates[S8]

$$\begin{aligned}
&\hat{H}\phi_{n,l}(\mathbf{r}_\parallel) = E_n\,\phi_{n,l}(\mathbf{r}_\parallel)\,, \qquad E_n = h\nu_c\left(n+\frac{1}{2}\right)\,, \quad n,\, l = 0,1,2,\ldots\,, \quad n_{l,\pm} = \frac{n+l\pm|n-l|}{2}\,,\\
&\phi_{n,l}(r,\varphi) = \mathcal{N}_{n,l}\,\mathrm{e}^{\mathrm{i}(n-l)\varphi}\,\mathrm{e}^{-\frac{1}{2}\left(\frac{r}{r_{\mathrm{c}}}\right)^2}\left(\frac{r}{r_{\mathrm{c}}}\right)^{|n-l|} L_{n_{l,-}}^{|n-l|}\left(\frac{r}{r_{\mathrm{c}}}\right)\,, \quad \mathcal{N}_{n,l}^2 \equiv \frac{1}{\pi r_{\mathrm{c}}^2}\frac{(n_{l,-})!}{(n_{l,+})!}\,,
\end{aligned} \tag{3}$$

where $L_l^n(x)$ is the associated Laguerre polynomial and $r_{\mathrm{c}} = \sqrt{\frac{2\hbar}{|e|B}}$ is the radius of the classical Landau orbit, defining the typical length scale of the system. We assume that the 2DEG is so strongly confined that it can be described via a strictly two-dimensional $\phi_{n,l}(\mathbf{r}_\parallel)$. Spatially, the peaks of $\phi_{n,l}(\mathbf{r}_\parallel)$ form rings whose size and width grows with increasing n (l) for a fixed l (n). The corresponding energy E_n contains the cyclotron frequency

$$\nu_c = \frac{1}{2\pi}\frac{|e|B}{m_e} \tag{4}$$

DOI: 10.1038/NPHYS3559

that depends only on the quantum number n such that each energy E_n has an infinite l degeneracy.

Intersubband coupling

In general, our system has multiple subbands and each of them carries its individual Landau ladder. In principle, the different subbands may be coupled via THz excitation directly or via Coulombic coupling that induces Auger-type particle exchange between the subbands. To verify that our experiment can be described by including only the ground-state subband in the many-body calculations, we will next show that intersubband coupling effects are negligible.

Based on the band offset energy diagram in Fig. S2b, we find that our 2DEGs have an energy spacing of 15.2 meV between the two lowest subbands. Since our THz photon energy of the THz pulse is roughly 6 meV, the intersubband transitions are excited very nonresonantly, which greatly suppresses them. Additionally, our excitation configuration eliminates the intersubband transitions completely even for a resonant excitation due to dipole selection rules: our THz field is aligned within the 2DEG plane while the intersubband dipole $\mathbf{d}_{\mathrm{ISB}}$ points perpendicular to it. Therefore, the $\mathbf{d}_{\mathrm{ISB}} \cdot \mathcal{E}_0$ driving term to the intersubband transitions vanishes for all photon energies, making intersubband transitions strictly forbidden in our setup. Appreciable intersubband transitions[S9,S10] in our excitation configuration can be induced by changing the propagation direction of the THz pulse by 90° degrees and increasing the THz-photon energy by a factor of three.

Consequently, only Auger-type Coulomb coupling may induce transitions between subbands in our experiment. To study this possibility, we compute the Coulomb matrix elements[S7]

$$V^{\lambda,\nu}_{\nu',\lambda'}(\mathbf{q}) = \int \mathrm{d}z\, \mathrm{d}z'\, \xi^{\star}_{\lambda}(z)\xi^{\star}_{\nu}(z')\, V_{\mathbf{q}}\, \xi_{\nu'}(z')\xi_{\lambda'}(z)\, \mathrm{e}^{-|\mathbf{q}||z-z'|} \tag{5}$$

between different subbands, where $\xi_\lambda(z)$ is the confinement function with subband index λ and $V_{\mathbf{q}} = \frac{e^2}{2\varepsilon_0\varepsilon_r S}\frac{1}{|\mathbf{q}|}$ is the Coulomb potential defined in terms of the two-dimensional wave vector $\mathbf{q}$, vacuum permittivity ϵ_0, the background dielectric constant $\epsilon_r = 11.1$, and the quantization area S. The confinement functions are computed based on the confinement potential of our structure shown in Fig. S2b. We compare the largest Auger-type matrix element $V_{\mathrm{Auger}} = V^{\mathrm{SB1,SB1}}_{\mathrm{SB1,SB2}}$ with the direct $V_{\mathrm{Auger}} = V^{\mathrm{SB1,SB1}}_{\mathrm{SB1,SB1}}$ one among subbands SB1 (ground state) and SB2 (excited state). Figure S7 presents the ratio $V_{\mathrm{Auger}}/V_{\mathrm{direct}}$ [solid (dashed) black line for $V_{\mathrm{Auger}} > 0$ ($V_{\mathrm{Auger}} < 0$)] as a function of electron momentum q. Within the scale relevant for LLs, V_{Auger} is roughly two orders of magnitude smaller than V_{direct}, which shows that also the Coulomb scattering between

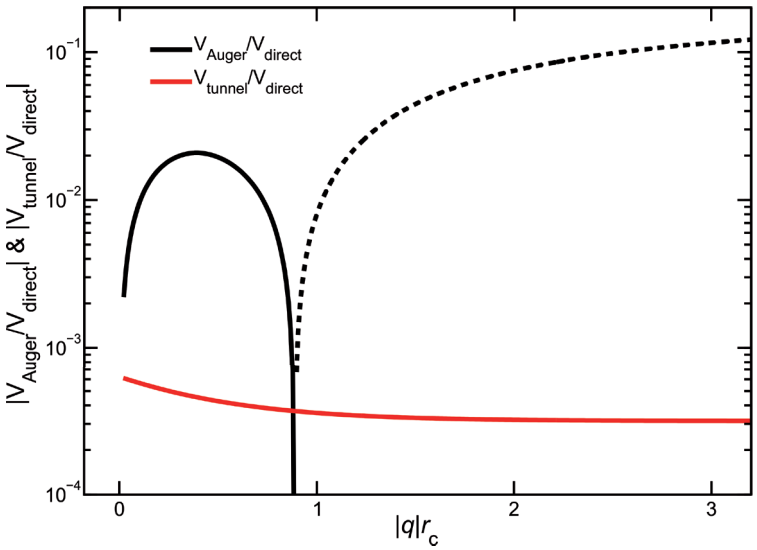

Figure S7 | Effect of Auger scattering and tunneling. The ratios $V_{\mathrm{Auger}}/V_{\mathrm{direct}}$ (solid (dashed) black line for $V_{\mathrm{Auger}} > 0$ ($V_{\mathrm{Auger}} < 0$)) and $V_{\mathrm{tunnel}}/V_{\mathrm{direct}}$ (red line) are shown as a function of electron momentum q.

the subbands is negligible in our system. Consequently, the consideration of a single subband in the many-body calculations is sufficient to describe our experiment.

Figure S7 also shows the ratio $V_{\mathrm{tunnel}}/V_{\mathrm{direct}}$ (red line) where V_{tunnel} is the Coulomb matrix element between electrons located at opposite sides of the tunneling barrier. It is even smaller than the Auger coupling, showing that also the tunneling has a negligible effect in our sample, as discussed in Supplementary Discussion 2.

Many-particle Hamiltonian

Many-particle properties of a 2DEG are described by introducing fermionic field operators $\hat{\Psi}^\dagger(\mathbf{r}_\parallel)$ and $\hat{\Psi}(\mathbf{r}_\parallel)$ that create and annihilate an electron at position $\mathbf{r}_\parallel$, respectively. We expand them in the Landau-level basis

$$\hat{\Psi}(\mathbf{r}_\parallel) = \sum_{n,l} a_{n,l}\, \phi_{n,l}(\mathbf{r}_\parallel)\,, \qquad \hat{\Psi}^\dagger(\mathbf{r}_\parallel) = \sum_{n,l} a^\dagger_{n,l}\, \phi^\star_{n,l}(\mathbf{r}_\parallel)\,, \tag{6}$$

DOI: 10.1038/NPHYS3559

where $a_{n,l}$ ($a^\dagger_{n,l}$) annihilates (creates) an electron in a Landau level (LL) with quantum numbers n and l. The many-body Hamiltonian in second quantization can then be written as

$$\begin{aligned}
\hat{H} &= \hat{H}_{\rm LL} + \hat{H}_{\rm ee} + \hat{H}_{\rm ion} + \hat{H}_{\rm lm}\,, \\
\hat{H}_{\rm LL} &= \sum_{n,l} E^\eta_n\, a^\dagger_{n,l} a_{n,l}\,, \quad \hat{H}_{\rm ee} = \frac{1}{2} \sum_{\substack{n,l,n',l' \\ m,j,m',j'}} V^{nl,mj}_{m'j',n'l'}\, a^\dagger_{n,l} a^\dagger_{m,j} a_{m',j'} a_{n',l'}\,, \\
\hat{H}_{\rm ion} &= -\rho_{\rm ion}\pi\, r_{\rm c}^2 \sum_{n,l,n',l',j} V^{nl,0j}_{0j,n'l'} a^\dagger_{n,l} a_{n',l'}\,, \quad \hat{H}_{\rm lm} = \sum_{n,l,n',l'} \mathcal{E}(t)\cdot \mathbf{d}^{n,l}_{n',l'} a^\dagger_{n,l} a_{n',l'}\,.
\end{aligned} \tag{7}$$

Since the anharmonic response in Fig. 2 of the main text may stem from the nonparabolic energy dispersion, we include the nonparabolicity to $\hat{H}_{\rm LL}$ via[S11]

$$E^\eta_n\,(1+\eta\,E^\eta_n) = E_n \tag{8}$$

with nonparabolicity parameter $\eta = 1.02\,{\rm eV}^{-1}$ for GaAs[S12].

The ions within the doping layer are assumed to form a uniform positive charge background with constant density $\rho_{\rm ion}$ which is assumed to be identical to the total electron density $\rho_{\rm e}$. The resulting electron–electron and electron–ion interactions are described by $\hat{H}_{\rm ee}$ and $\hat{H}_{\rm ion}$, respectively. They contain the Coulomb matrix element

$$V^{nl,mj}_{m'j',n'l'} \equiv \int {\rm d}^2 r_\parallel \int {\rm d}^2 r'_\parallel\, \phi^\star_{n,l}(\mathbf{r}_\parallel)\phi^\star_{m,j}(\mathbf{r}'_\parallel) \sum_{\mathbf{q}} V_{\mathbf{q}}\, {\rm e}^{{\rm i}\mathbf{q}\cdot(\mathbf{r}_\parallel - \mathbf{r}'_\parallel)} \phi_{m',j'}(\mathbf{r}'_\parallel)\phi_{n',l'}(\mathbf{r}_\parallel)\,. \tag{9}$$

In general, $V^{nl,mj}_{m'j',n'l'}$ can be analytically computed in terms of finite sums[S13]. However, the resulting expression is inappropriate for numerical calculations with large LL quantum numbers. To efficiently determine $V^{nl,mj}_{m'j',n'l'}$, we perform the $\mathbf{q}$-sum numerically after we evaluate only the $\mathbf{r}_\parallel$ and $\mathbf{r}'_\parallel$ integrals analytically, producing

$$V^{n_1 l_1, n_2 l_2}_{n_3 l_3, n_4 l_4} = (-1)^{n_1+n_3-l_2-l_4} \delta_{\substack{n_1+n_2-l_1-l_2,\\ n_3+n_4-l_3-l_4}} \sum_{\mathbf{q}} V_{\mathbf{q}}\, M_{n_1,n_4}(\mathbf{q}) M_{n_2,n_3}(\mathbf{q}) M_{l_1,l_4}(\mathbf{q}) M_{l_2,l_3}(\mathbf{q}) \tag{10}$$

with

$$M_{l,l'}(\mathbf{q}) \equiv \sqrt{l!l'!}\,{\rm e}^{-\frac{|\mathbf{q}|^2}{8}} \sum_{L=0}^{\min[l,l']} \frac{(-1)^L \left(\frac{|\mathbf{q}|}{2}\right)^{l+l'-2L}}{L!(l-L)!(l'-L)!}\,. \tag{11}$$

This strategy yields accurate Coulomb matrix elements even for large quantum numbers n and l. Nevertheless, $V^{n_1 l_1, n_2 l_2}_{n_3 l_3, n_4 l_4}$ has in general more than 10^{10} elements which makes the calculations numerically demanding.

The light–matter coupling $\hat{H}_{\rm lm}$ between the THz field and the 2DEG is defined in the $\mathbf{r}\cdot\mathcal{E}$-picture[S7]. The classical THz field is assumed to propagate in z-direction, i. e. perpendicular to the 2DEG. As in the experiment, the electric field $\mathcal{E}(t)$ is linearly polarised in x-direction for the single THz excitation setup while the probe (pump) pulse is linearly polarised in y-direction (x-direction) in the wave-mixing investigations. The corresponding THz dipole matrix elements are

$$\begin{aligned} d^{n,l}_{n',l'}|_x &= -\frac{|e|r_{\rm c}}{2}\left[\delta_{l,l'}\left(\delta_{n',n-1}\sqrt{n}+\delta_{n',n+1}\sqrt{n+1}\right)+\delta_{n,n'}\left(\delta_{l',l-1}\sqrt{l}+\delta_{l',l+1}\sqrt{l+1}\right)\right], \\ d^{n,l}_{n',l'}|_y &= -\mathrm{i}\frac{|e|r_{\rm c}}{2}\left[\delta_{l,l'}\left(\delta_{n',n+1}\sqrt{n+1}-\delta_{n',n-1}\sqrt{n}\right)+\delta_{n,n'}\left(-\delta_{l',l+1}\sqrt{l+1}+\delta_{l',l-1}\sqrt{l}\right)\right] \end{aligned} \tag{12}$$

in x- and y-direction, respectively.

5. Kohn's theorem

To study the origin of the measured $\nu_{\rm c}$-changes, we investigate the dynamics of the macroscopic polarisation operator[S7]

$$\hat{\mathbf{P}} = \frac{\sigma N_{\rm 2DEG}}{\varepsilon_0\, S\, L_{\rm 2DEG}} \sum_{n,l,n',l'} \mathbf{d}^{n,l}_{n',l'} a^\dagger_{n,l} a_{n',l'}\,, \tag{13}$$

where $N_{\rm 2DEG}=2$ is the number of 2DEGs, $\sigma=2$ accounts for the spin degeneracy, and $L_{\rm 2DEG}$ is the finite width of the 2DEG quantum well. The corresponding canonical macroscopic current operator is[S7]

$$\hat{\mathbf{J}} = -\frac{\sigma N_{\rm 2DEG}}{\varepsilon_0\, S\, L_{\rm 2DEG}} \int \mathrm{d}^2 r_\parallel\, \hat{\Psi}^\dagger(\mathbf{r}_\parallel)\frac{|e|}{m_{\rm e}}\left(\hat{\mathbf{p}}+|e|\mathbf{A}_{\rm stat}(\mathbf{r})\right)\hat{\Psi}(\mathbf{r}_\parallel)\,. \tag{14}$$

Since we want to determine why the Coulomb interaction alone violates Kohn's theorem, we neglect the nonparabolicity in this section by setting $\eta=0$ in Eq. (8). We first compute the $\hat{\mathbf{P}}=(\hat{P}_x,\hat{P}_y)$

DOI: 10.1038/NPHYS3559

and $\hat{\mathbf{J}} = (\hat{J}_x, \hat{J}_y)$ dynamics without $\hat{H}_{\rm ion}$ by evaluating the Heisenberg equation of motion:

$$\begin{aligned}
\frac{\partial}{\partial t}\hat{\mathbf{P}}|_{\rm w/o\,ion} &\equiv \frac{\mathrm{i}}{\hbar}\left[\hat{H}_{\rm LL}+\hat{H}_{\rm ee}+\hat{H}_{\rm lm},\hat{\mathbf{P}}\right]_{\eta=0} = \hat{\mathbf{J}}\,,\\
\frac{\partial}{\partial t}\hat{J}_x|_{\rm w/o\,ion} &\equiv \frac{\mathrm{i}}{\hbar}\left[\hat{H}_{\rm LL}+\hat{H}_{\rm ee}+\hat{H}_{\rm lm},\hat{J}_x\right]_{\eta=0} = -\omega_{\rm c}\hat{J}_y+\omega_{\rm pl}\mathcal{E}_x\,,\\
\frac{\partial}{\partial t}\hat{J}_y|_{\rm w/o\,ion} &\equiv \frac{\mathrm{i}}{\hbar}\left[\hat{H}_{\rm LL}+\hat{H}_{\rm ee}+\hat{H}_{\rm lm},\hat{J}_y\right]_{\eta=0} = \omega_{\rm c}\hat{J}_x+\omega_{\rm pl}\mathcal{E}_y\,,
\end{aligned} \tag{15}$$

where $\omega_{\rm pl}^2 = \frac{|e|^2\rho_{\rm 3D}}{\varepsilon_0 m_{\rm e}}$ is the plasma frequency with a 3D electron density $\rho_{\rm 3D} = \rho_{\rm e}/L_{\rm 2DEG}$. Equation (15) implies that the $\hat{\mathbf{P}}$ and $\hat{\mathbf{J}}$ dynamics has no trace of the electron–electron Coulomb interaction and the dynamics is closed at the operator level. In particular, Eq. (15) forms a linearly coupled operator pair $(\hat{\mathbf{P}},\hat{\mathbf{J}})$ whose resonance frequency is defined by an excitation-independent cyclotron frequency $\omega_{\rm c} = 2\pi\nu_{\rm c}$, which is the main aspect of Kohn's theorem[2]. Physically, the operator dynamics (15) for the current describes a driven (classical) harmonic oscillator and it is exactly solvable. Since harmonic systems have no nonlinearities, the 2DEG behaves classically as long as nonparabolicity and electron–ion Coulomb interaction are ignored. Therefore, electron–electron interactions alone cannot produce observable nonlinearities or quantum behaviour in a 2DEG when it is placed inside a static magnetic field.

The situation changes when the electron–ion interaction is included because

$$\begin{aligned}
\frac{\partial}{\partial t}\hat{P}_x|_{\rm ion} \equiv \frac{\mathrm{i}}{\hbar}\left[\hat{H}_{\rm ion},\hat{P}_x\right] &= \mathrm{i}\frac{|e|\rho_{\rm ion}\pi r_{\rm c}^3}{2\hbar S}\sum_{\substack{n_1,l_1,\\ n_2,l_2,l_3}}\Big(\sqrt{n_1+1}\,V_{0,l_3,n_2,l_2}^{n_1+1,l_1,0,l_3}-\sqrt{n_2}\,V_{0,l_3,n_2-1,l_2}^{n_1,l_1,0,l_3}\\
&\quad+\sqrt{l_1+1}\,V_{0,l_3,n_2,l_2}^{n_1,l_1+1,0,l_3}-\sqrt{l_2}\,V_{0,l_3,n_2,l_2-1}^{n_1,l_1,0,l_3}\Big)\,a_{n,l}^{\dagger}a_{n',l'}+\text{h. c.}\,,\\
\frac{\partial}{\partial t}\hat{P}_y|_{\rm ion} \equiv \frac{\mathrm{i}}{\hbar}\left[\hat{H}_{\rm ion},\hat{P}_y\right] &= \frac{|e|\rho_{\rm ion}\pi r_{\rm c}^3}{2\hbar S}\sum_{\substack{n_1,l_1,\\ n_2,l_2,l_3}}\Big(\sqrt{n_1+1}\,V_{0,l_3,n_2,l_2}^{n_1+1,l_1,0,l_3}-\sqrt{n_2}\,V_{0,l_3,n_2-1,l_2}^{n_1,l_1,0,l_3}\\
&\quad-\sqrt{l_1+1}\,V_{0,l_3,n_2,l_2}^{n_1,l_1+1,0,l_3}+\sqrt{l_2}\,V_{0,l_3,n_2,l_2-1}^{n_1,l_1,0,l_3}\Big)\,a_{n,l}^{\dagger}a_{n',l'}+\text{h. c.}\,,
\end{aligned} \tag{16}$$

couples the macroscopic $\hat{\mathbf{P}}$ (and $\hat{\mathbf{J}}$) to a new class of Coulomb terms, not expressible in terms of $\hat{\mathbf{P}}$ and $\hat{\mathbf{J}}$. As a result, the electron–ion interaction modifies the $\hat{\mathbf{P}}$ and $\hat{\mathbf{J}}$ dynamics and thus breaks the $\nu_{\rm c}$-conservation, which alone induces a nonlinear 2DEG response once the electric field becomes strong enough, as demonstrated in the main text. Consequently, a full many-body theory including the electron–ion interaction is needed to explain the experimental observations.

6. Equations of motion

To analyze the consequences of $\hat{H}_{\rm ion}$, we compute the dynamics of the microscopic expectation values $p^{n,l}_{n',l'} \equiv \langle a^\dagger_{n,l} a_{n',l'} \rangle$ to deduce the macroscopic polarization response. For $n = n'$ and $l = l'$, $p^{n,l}_{n,l}$ defines the electronic occupation of LL $\phi_{n,l}$. As a result, the total occupation of LL n and electron density follows from

$$f(n) = \sum_l p^{n,l}_{n,l}\,, \qquad \rho_{\rm e} = \frac{\sigma N_{\rm 2DEG}}{S} \sum_n f(n)\,, \tag{17}$$

respectively. All other $p^{n,l}_{n',l'}$ combinations with $n \neq n'$ or $l \neq l'$ describe microscopic polarizations between different LLs.

To define the initial $p^{n,l}_{n',l'}$, we assume that the electron density

$$\rho(\mathbf{r}_\parallel) = \langle \Psi^\dagger(\mathbf{r}_\parallel)\Psi(\mathbf{r}_\parallel)\rangle = \sum_{n,l,n',l'} p^{n,l}_{n',l'} \phi^\star_{n,l}(\mathbf{r}_\parallel)\phi_{n',l'}(\mathbf{r}_\parallel) \tag{18}$$

is homogeneous. Due to the sample temperature of $T = 4.3\,{\rm K}$ and $\rho_{\rm e} = 3.2 \times 10^{11}\,{\rm cm}^{-2}$, essentially all electrons occupy the ground state $n = 0$. For our calculations, we choose a constant occupation $p^{n,l}_{n',l'} = \delta_{n,n'}\delta_{l,l'} f_0$ of the ground state which produces a homogeneous density $\rho(\mathbf{r}_\parallel) = \frac{\sigma\, N_{\rm 2DEG}}{\pi r_{\rm c}^2} f_0$ within the entire 2D space. This connection can be inverted to deduce $f_0 = \pi r_{\rm c}^2 \rho_{\rm e}/(\sigma\, N_{\rm 2DEG}) = 0.95$.

We apply the cluster expansion[S7] to derive the semiconductor Bloch equations for a 2DEG in a static magnetic field

$$\begin{aligned}
{\rm i}\hbar \frac{\partial}{\partial t} p^{N,L}_{N',L'} &= \left(E^\eta_{N'} - E^\eta_N\right) p^{N,L}_{N',L'} + \sum_{n,l} \left(H^{N',L'}_{n,l} p^{N,L}_{n,l} - H^{n,l}_{N,L} p^{n,l}_{N',L'} - F^{N',L'}_{n,l} p^{N,L}_{n,l} + F^{n,l}_{N,L} p^{n,l}_{N',L'} \right) \\
&+ \rho_{\rm ion} \pi\, r_{\rm c}^2 \sum_{n,l,l'} \left(V^{nl,0l'}_{0l',NL} p^{n,l}_{N',L'} - V^{N'L',0l'}_{0l',nl} p^{N,L}_{n,l} \right) \\
&+ \mathcal{E}_x(t) \Big[d_{N'} p^{N,L}_{N'-1,L'} + d_{N'+1} p^{N,L}_{N'+1,L'} + d_{L'} p^{N,L}_{N',L'-1} + d_{L'+1} p^{N,L}_{N',L'+1} \\
&\qquad - d_N p^{N-1,L}_{N',L'} - d_{N+1} p^{N+1,L}_{N',L'} - d_L p^{N,L-1}_{N',L'} - d_{L+1} p^{N,L+1}_{N',L'} \Big] \\
&+ {\rm i}\mathcal{E}_y(t) \Big[d_{N'+1} p^{N,L}_{N'+1,L'} - d_{N'} p^{N,L}_{N'-1,L'} + d_{L'} p^{N,L}_{N',L'-1} - d_{L'+1} p^{N,L}_{N',L'+1} \\
&\qquad + d_{N+1} p^{N+1,L}_{N',L'} - d_N p^{N-1,L}_{N',L'} + d_L p^{N,L-1}_{N',L'} - d_{L+1} p^{N,L+1}_{N',L'} \Big] + D^{N,L}_{N',L'}
\end{aligned} \tag{19}$$

DOI: 10.1038/NPHYS3559

with

$$H^{N,L}_{N',L'} \equiv \sum_{n,l,n',l'} V^{NL,nl}_{n'l',N'L'} p^{n,l}_{n',l'}\,, \qquad F^{N,L}_{N',L'} \equiv \sum_{n,l,n',l'} V^{nl,NL}_{n'l',N'L'} p^{n,l}_{n',l'}\,, \quad d_N \equiv \frac{|e|r_c}{2}\sqrt{N}\,, \tag{20}$$

where $D^{N,L}_{N',L'}$ stems from two-particle cluster due to Coulomb and phonon interactions and we approximate it with $D^{N,L}_{N',L'} = -\mathrm{i}\gamma_{N,N'} p^{N,L}_{N',L'}$ where $\gamma_{N,N'}$ includes excitation-induced dephasing, as discussed in Supplementary Discussion 10.

7. Description of excitation in a finite excitation spot

Since the THz pulses in the experiment are focused to a finite excitation spot, the $p^{n,l}_{n',l'}$ excitations extend only over a finite region. The l-states and spatial extension are uniquely connected; the radius of the excitation is given by $r = \sqrt{N_l}\, r_c$ where only $l = 0, 1, \ldots, N_l$ states become excited. At the same time, the range n is limited by the strength of the excitation because increasing n-states are realized only via multi-photon absorption. With these considerations, the LL *excitations* can be limited in both l and n quantum numbers. For our numerical evaluations, we have used up to 15 n-states and $N_l = 100$, which means that we follow the quantum kinetics of $(15\times100)^2 = 2.25\times10^6$ $p^{n,l}_{n',l'}$ elements, which is numerically very demanding. We have carefully checked that this amount of n- and l-states yields size-independent results, as shown in Supplementary Discussion 8.

Due to the finite l range, it is useful to express the excitation via

$$p^{n,l}_{n',l'} = \delta_{n,0}\,\delta_{n',0}\,\delta_{l,l'}\,f_0\,\theta(l-N_l) + p^{n,l}_{n',l'}\theta(N_l-l)\,, \tag{21}$$

because $p^{n,l}_{n',l'}$ becomes the ground-state occupation outside the excitation spot; the Heaviside-theta function $\theta(x)$ simply provides the inside ($\theta(N_l-l)$) outside ($\theta(l-N_l)$) devision. To gain numerical accuracy in the computations, it is beneficial to use a smoothly changing excitation spot. Since l and the radial dependencies are connected, a finite and smoothly changing excitation spot can be realized by introducing an l, l' dependence to $\mathcal{E}_x$ and $\mathcal{E}_y$. This procedure is equivalent to replacing $p^{n,l}_{n',l'}$ by

$$\tilde{p}^{n,l}_{n',l'} = G(l)\, p^{n,l}_{n',l'}\, G(l')\,, \quad G(l) = \frac{1}{\mathrm{e}^{(l_{\mathrm{exc}}-l)/\Delta l}+1} \tag{22}$$

at the right-hand side of Eq. (21). In $G(l)$, l_{exc} defines the half-width of the excitation spot with area $S_{\mathrm{exc}} = \pi\, r_c^2\, l_{\mathrm{exc}}$ and steepness Δl. The replacement (22) also smoothly switches off the

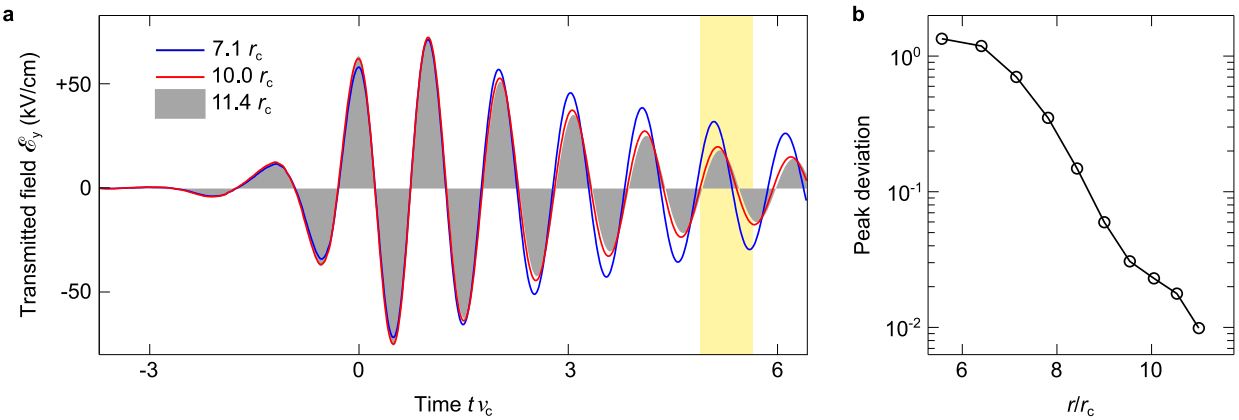

Figure S8 | Convergence of macroscopic response. a, The dynamics of the transmitted electric field $\mathcal{E}_{\mathrm{trans},y}(t)$ is shown for a spot size of $r = 7.1\,r_c$ (cyan line), $r = 10.0\,r_c$ (red line), and $r = 11.4\,r_c$ (shaded area); the THz field amplitude is $\mathcal{E}_0 = 5.7\,\mathrm{kV/cm}$ while the nonparabolicity is $\eta = 1.02\,\mathrm{eV}^{-1}$. **b**, Relative deviation $\varepsilon_{\mathrm{dev}}(r)$ as a function of spot radius r. The studied peak is indicated by a shaded area in **a**.

Coulomb interaction outside the excitation spot, which further helps to improve the convergence in the numerics. At the same time, it fully conserves Kohn's theorem (15).

8. Independence of THz response of spot size

To obtain the macroscopic THz response, we compute the macroscopic polarization $\mathbf{P}(t) = \langle\hat{\mathbf{P}}(t)\rangle$ which defines the transmitted electrical field at the position of a planar 2DEG[S7] via

$$\mathcal{E}_{\mathrm{trans}}(t) = \mathcal{E}(t) - \mu_0 \frac{c}{2\sqrt{\varepsilon_r}} \frac{\partial}{\partial t}\mathbf{P}(t)\,, \tag{23}$$

where $\mathcal{E}(t)$ is the incoming THz field, μ_0 denotes the vacuum permeability, and c is the speed of light. For the excitation configuration described in Sec. 7, the macroscopic polarization is

$$\mathbf{P}(t) = \frac{\sigma\, N_{\mathrm{2DEG}}}{S_{\mathrm{exc}}} \sum_{n,l,n',l'} \mathbf{d}^{n,l}_{n',l'} \tilde{p}^{n,l}_{n',l'} \tag{24}$$

after we include a smoothly changing spot via Eq. (22).

Due to computational restrictions, the numerical computations cannot use the large l_{exc} value of the experiment. However, the system response approaches a homogeneous response as the spot size becomes sufficiently large. To check that we are indeed in this limit, we compute $\mathcal{E}_{\mathrm{trans},y}(t)$ for N_l ranging from 30 to 130 and choose $l_{\mathrm{exc}} = N_l - 20$. Figure S8a presents $\mathcal{E}_{\mathrm{trans},y}(t)$ for a spot

DOI: 10.1038/NPHYS3559

size of $7.1\,r_c$ ($N_l = 30$, cyan line), $10.0\,r_c$ ($N_l = 100$, red line), and $11.4\,r_c$ ($N_l = 130$, shaded area) used in the computations; the THz field amplitude is $\mathcal{E}_0 = 5.7\,\mathrm{kV/cm}$. We see that the response converges excellently with increasing spot size which shows that we can accurately describe the experiment with a relatively small l_{exc}. To quantify the convergence in more detail, we study the relative deviation

$$\varepsilon_{\mathrm{dev}}(r) = \frac{|\mathcal{E}_{\mathrm{peak}}(r) - \mathcal{E}_{\mathrm{peak}}(r_{\mathrm{max}})|}{\mathcal{E}_{\mathrm{peak}}(r_{\mathrm{max}})} \tag{25}$$

of the peak $\mathcal{E}_{\mathrm{peak}}$ defined within a time window indicated by the shaded area in Fig. S8a. The reference $r_{\mathrm{max}} = 11.4\,r_c$ is the largest r used in the calculations. Figure S8b shows $\varepsilon_{\mathrm{dev}}(r)$ as a function of r. The result is roughly exponentially converging such that $r = 10\,r_c$ ($N_l = 100$) is sufficient to describe measurements accurately. We use $N_l = 100$ in our computations in the main text.

9. Coulomb effects on initial state and Kohn's theorem

Without any excitation, the electron–electron interaction described by the second term in Eq. (19) creates a very strong repulsion among the electrons, and thus pushes the 2DEG electrons towards an inhomogeneous Wigner crystal[S14,S15] within the 2DEG. However, this repulsive interaction is balanced by the electron–ion interaction represented by the third term of Eq. (19), which leads to an effectively evenly distributed electron cloud within the 2DEG. To illustrate this behavior, we start from an initially homogeneous $\rho(\mathbf{r}_\parallel)$ and compute the kinetics of $\rho(\mathbf{r}_\parallel)$ with and without electron–ion Coulomb interaction. Figure S9 shows $\rho(\mathbf{r}_\parallel)$ after 4.8 ps (a), 8.8 ps (b), and 35.5 ps (c) of the dynamical evolution. A calculation without electron–ion interaction (black line) is compared with a full computation (red line); shaded areas indicate the edges of l_{exc} (inner) and N_l (outer). The computation without electron–ion interaction produces a strong inhomogeneous redistribution of electrons resembling the formation of a Wigner crystal. However, the electron–ion interaction balances the electron–electron repulsion and produces a very homogeneous $\rho(\mathbf{r}_\parallel)$ for all times. Only some residual wiggles are present, indicating that the assumed smooth ion distribution is sufficient to produce a reasonably homogeneous 2DEG. These wiggles vanish exponentially as ρ_{exc} is increased such that they have no experimentally observable effects.

To verify that $\hat{H}_{\mathrm{ee}}$ does not modify the macroscopic polarization while $\hat{H}_{\mathrm{ion}}$ violates Kohn's theorem, Fig. S10a shows the computed $P_y(t)$ for a calculation without Coulomb interaction (shaded

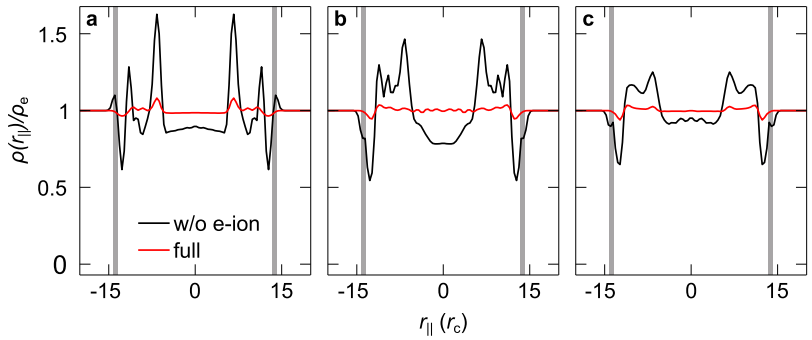

Figure S9 | Effect of electron–ion Coulomb interaction. a, The electron density $\rho(r_\parallel)/\rho_e$ is shown after 4.8 ps of the dynamical evolution, starting from an initially homogeneous $\rho(\mathbf{r}_\parallel)$. The result without electron–ion interaction (black line) is compared with the result of a full computation (red line); shaded areas indicate the edges of l_{exc} (inner) and N_l (outer). The corresponding results for the times 8.8 ps and 35.5 ps are plotted in **b** and **c**, respectively.

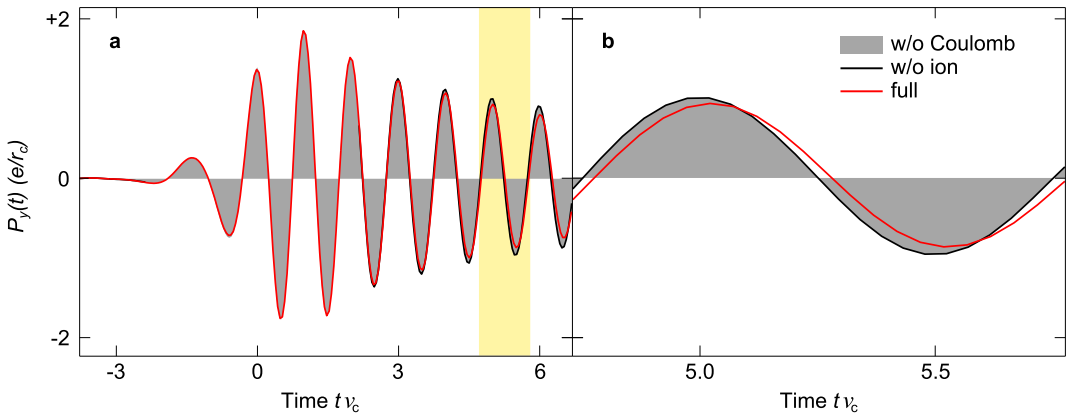

Figure S10 | Coulomb effects on macroscopic response. a, The macroscopic polarization $P_y(t)$ of a calculation without Coulomb interaction (shaded area) is compared to an analysis without electron–ion interaction (black line) and a full calculation (red line); the THz field amplitude is $\mathcal{E}_0 = 5.7\,\mathrm{kV/cm}$ while the nonparabolicity is $\eta = 0$. **b**, Magnification of **a** at late times indicated by a shaded area in **a**.

area), without $\hat{H}_{\mathrm{ion}}$ (black line), and for a full computation (red line); the field amplitude is $\mathcal{E}_0 = 5.7\,\mathrm{kV/cm}$ and the calculations have been performed for a parabolic energy dispersion, i. e. $\eta = 0$ in Eq. (8). A magnification of an oscillation cycle is plotted in Fig. S10b indicated by a shaded area in Fig. S10a to have a simpler interpretation of the results. The computation without $\hat{H}_{\mathrm{ion}}$ reproduces the calculation without Coulomb interaction such that the electron–electron Coulomb interaction indeed conserves the macroscopic polarization in agreement with Kohn's theorem. This also verifies the consistency of our numerics. At the same time, $\hat{H}_{\mathrm{ion}}$ induces ν_c-changes even without nonparabolicity, yielding pronounced nonlinearities in the strong excitation regime.

DOI: 10.1038/NPHYS3559

10. Phonon scattering and excitation-induced dephasing

For the dephasing we use $\gamma_{n,n'} = \frac{\Gamma_n + \Gamma_{n'}}{2}$ with $\Gamma_n = \gamma_n(1 + \gamma_{\mathrm{EID}})$ on the right-hand side of the equation-of-motion (19). The LO phonon scattering is described by Γ_n which is $1/\gamma_n = 9.0\,\mathrm{ps}$ for $n \leq 5$ and $1/\gamma_n = 0.8\,\mathrm{ps}$ for $n > 5$.

Besides the anharmonic response beyond Kohn's theorem, we also identify excitation-induced dephasing (EID)[S7,S16,S17] as an additional Coulomb-induced effect. In the low excitation regime, all electrons occupy only the ground-state LL $n = 0$ and all l states are occupied evenly such that the Coulombic in- and out-scattering processes of the electrons fully compensate each other, yielding vanishing Coulomb-induced dephasing. However, our strong THz fields excite a majority of electrons to an uneven spread of l states, inducing an imbalance between in- and out-scattering, which leads to an additional dephasing. The dephasing γ_{EID} can be determined directly from the four-wave mixing measurements because EID mainly influences the decay of the nonlinear response as a function of pump–probe delay. Therefore, we determine the decay of the measured nonlinear response in Fig. 3 of the main text as a function of delay time for different THz field amplitudes which defines Γ experimentally. Figure S11a shows the resulting Γ (dots) as a function of THz field amplitude $\mathcal{E}_0$.

To model EID, we determine how Γ changes as a function of the excited carrier density

$$\rho_{\mathrm{exc}} = \frac{\sigma\, N_{\mathrm{2DEG}}}{S} \sum_{n>0} f(n)\,, \tag{26}$$

and compute ρ_{exc} as a function of $\mathcal{E}_0$. The result is shown in Fig. S11b where ρ_{exc} is plotted as a function of $\mathcal{E}_0$. We see that ρ_{exc} grows with increasing $\mathcal{E}_0$, peaking at $0.79\ \rho_{\mathrm{e}}$. By combining the experimentally deduced Γ and the computed ρ_{exc}, we find that γ_{EID} is essentially proportional to the square of ρ_{exc}

$$\gamma_{\mathrm{EID}} = \kappa\,(\rho_{\mathrm{exc}} - \rho_{\mathrm{thres}})^2\,\theta(\rho_{\mathrm{exc}} - \rho_{\mathrm{thres}})\,, \tag{27}$$

where κ defines the strength of the EID. The Heaviside function takes into account that the EID only becomes efficient when the excited carrier density exceeds a threshold density ρ_{thres}. The fitted γ_{EID} (red line) is compared with the experimental Γ (dots) in Fig. S10a. The experimental result is well reproduced by $\kappa = 17.0/\rho_{\mathrm{e}}^2$ and $\rho_{\mathrm{thres}} = 0.1\,\rho_{\mathrm{e}}$. In general, EID also contains an additional contribution from coherences due to polarization–polarization scattering. However, this

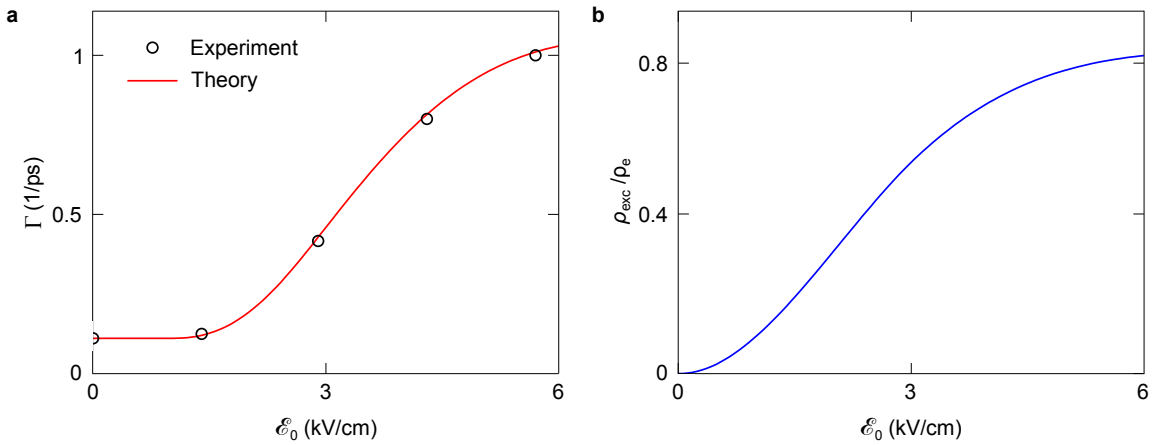

Figure S11 | Identification of excitation-induced dephasing. a, The decay Γ extracted from the measured (dots) and computed (red line) nonlinear response $\mathcal{E}_{\mathrm{NL}}(t,\tau)$ is shown as a function of field amplitude $\mathcal{E}_0$. **b**, Computed excitation density ρ_{exc} as a function of $\mathcal{E}_0$.

is not relevant once the coherences have decayed such that we omit the polarization–polarization scattering in the calculations.

11. Classical model

To study the limitations of Kohn's theorem, we also perform a classical calculation including a nonparabolic energy dispersion. We start from the minimal-substitution Hamiltonian

$$H = \frac{\left(\mathbf{p} + |e|\mathbf{A}(\mathbf{r},t)\right)^2}{2m_{\mathrm{e}}} - \eta\frac{\left(\mathbf{p} + |e|\mathbf{A}(\mathbf{r},t)\right)^4}{4m_{\mathrm{e}}^2}\,, \tag{28}$$

where the electromagnetic field is described by the vector potential $\mathbf{A}(\mathbf{r},t)$ while the second contribution accounts for the nonparabolic energy dispersion. By applying Hamilton's equation of motion and using the Lorentz force $\mathbf{F}(\mathbf{r},t) = -|e|(\mathbf{v}\times\mathbf{B}(\mathbf{r}) + \mathcal{E}(t))$, we obtain a closed set of coupled equations for the current density $\mathbf{J}(t)$

$$\begin{aligned}
\frac{\partial J_x(t)}{\partial t} &= \frac{|e|^2\rho_{\mathrm{e}}}{m_{\mathrm{e}}}\bar{\eta}(t)\mathcal{E}_x(t) - \omega_{\mathrm{c}}\bar{\eta}(t)J_y(t) + \eta\frac{2m_{\mathrm{e}}}{\rho_{\mathrm{e}}}\frac{1}{\bar{\eta}^2(t)}J_x(t)\left(J_x(t)\mathcal{E}_x(t) + J_y(t)\mathcal{E}_y(t)\right) - \mathrm{i}\gamma_{\mathrm{cl}}J_x(t)\,,\\
\frac{\partial J_y(t)}{\partial t} &= \frac{|e|^2\rho_{\mathrm{e}}}{m_{\mathrm{e}}}\bar{\eta}(t)\mathcal{E}_y(t) + \omega_{\mathrm{c}}\bar{\eta}(t)J_x(t) + \eta\frac{2m_{\mathrm{e}}}{\rho_{\mathrm{e}}}\frac{1}{\bar{\eta}^2(t)}J_y(t)\left(J_x(t)\mathcal{E}_x(t) + J_y(t)\mathcal{E}_y(t)\right) - \mathrm{i}\gamma_{\mathrm{cl}}J_y(t)\,,\\
\frac{\partial\bar{\eta}(t)}{\partial t} &= \eta\frac{2m_{\mathrm{e}}}{\rho_{\mathrm{e}}}\frac{1}{\bar{\eta}(t)}\left(J_x(t)\mathcal{E}_x(t) + J_y(t)\mathcal{E}_y(t)\right)\,,
\end{aligned} \tag{29}$$

DOI: 10.1038/NPHYS3559

where $\bar{\eta}$ describes the average nonparabolicity and $\gamma_{\mathrm{cl}} = 1/(9.0\,\mathrm{ps})$ is a constant phenomenological damping. The transmitted electric field at the position of the 2DEG follows from Eq. (23) by using $\mathbf{J}(t) = \frac{\partial \mathbf{P}(t)}{\partial t}$.

S1. Hebling, J., Almasi, G., Kozma, I. & Kuhl, J. Velocity matching by pulse front tilting for large area THz-pulse generation. *Opt. Express* **10**, 1161–1166 (2002).

S2. Planken, P. C. M., Nienhuys, H.-K., Bakker, H. J. & Wenckebach, T. Measurement and calculation of the orientation dependence of terahertz pulse detection in ZnTe. *J. Opt. Soc. Am. B* **18**, 313–317 (2001).

S3. Arikawa, T. *et al.* Quantum control of a Landau-quantized two-dimensional electron gas in a GaAs quantum well using coherent terahertz pulses. *Phys. Rev. B* **84**, 241307 (2011).

S4. Vurgaftman, I., Meyer, J. R. & Ram-Mohan, L. R. Band parameters for III–V compound semiconductors and their alloys. *Journal of Applied Physics* **89**, 5815–5875 (2001).

S5. Kuehn, W., Reimann, K., Woerner, M. & Elsaesser, T. Phase-resolved two-dimensional spectroscopy based on collinear n-wave mixing in the ultrafast time domain. *The Journal of Chemical Physics* **130**, 164503 (2009).

S6. Haug, H. & Koch, S. W. *Quantum Theory of the Optical and Electronic Properties of Semiconductors* (World Scientific, 2009).

S7. Kira, M. & Koch, S. W. *Semiconductor Quantum Optics* (Cambridge University Press, 2011).

S8. Cohen-Tannoudji, C., Diu, B. & Laloe, F. *Quantum Mechanics* (Wiley, 1991).

S9. Schlesinger, Z., Hwang, J. C. M. & Allen, S. J. Subband-Landau-level coupling in a two-dimensional electron gas. *Phys. Rev. Lett.* **50**, 2098–2101 (1983).

S10. Wieck, A. D. *et al.* Subband-Landau-level coupling in GaAs/$Ga_{1-x}Al_xAs$ heterojunctions. *Phys. Rev. B* **39**, 3785–3794 (1989).

S11. Blanchard, F. *et al.* Effective mass anisotropy of hot electrons in nonparabolic conduction bands of *n*-doped InGaAs films using ultrafast terahertz pump-probe techniques. *Phys. Rev. Lett.* **107**, 107401 (2011).

S12. Pfeffer, P. & Zawadzki, W. Five-level $\mathbf{k}\cdot\mathbf{p}$ model for the conduction and valence bands of GaAs and InP. *Phys. Rev. B* **53**, 12813–12828 (1996).

S13. Mondragon-Shem, I., Rodrguez, B. A. & López, F. E. Efficient calculation of Coulomb matrix elements for bilayers of confined charge carriers with arbitrary spatial separation. *Computer Physics Communications* **181**, 1510–1516 (2010).

S14. Goldman, V., Santos, M. & Shayegan, M. Evidence for two-dimensional quantum Wigner crystal. *Phys. Rev. Lett.* **65**, 2189–2192 (1990).

S15. Filinov, A. V., Bonitz, M. & Lozovik, Y. E. Wigner crystallization in mesoscopic 2d electron systems. *Phys. Rev. Lett.* **86**, 3851–3854 (2001).

S16. Kira, M. & Koch, S. W. Many-body correlations and excitonic effects in semiconductor spectroscopy. *Prog. Quantum Electron* **30**, 155–296 (2006).

S17. Smith, R. P. *et al.* Extraction of many-body configurations from nonlinear absorption in semiconductor quantum wells. *Phys. Rev. Lett.* **104**, 247401 (2010).